Constructing reconstruction-inhibited nickel selenide electrocatalysts via incorporating Ag single atom for durable and efficient water oxidation

Fangqing Wang [a,b,1], Xueru Zhao [c,1], Ying Li [a,b], Limin Liang [a,b], Kotaro Sasaki [c], Qiuyan Hao [a,b], Wenhao Yuan [d], Sijia Li [a,b,*], Hui Liu [a,b,*]

[a] Key Laboratory of Special Functional Materials for Ecological Environment and Information (Ministry of Education), Hebei University of Technology, Tianjin 300130, PR China
[b] School of Material Science and Engineering, Hebei University of Technology, Tianjin 300130, PR China
[c] Chemistry Department, Brookhaven National Laboratory, Upton, NY 11973, USA
[d] Department of Material Science and Engineering, College of Design and Engineering, National University of Singapore, Singapore 117575, Singapore

ARTICLE INFO

ABSTRACT

Transition-metal selenides exhibit excellent catalytic activity towards oxygen evolution reaction (OER), but suffering from serious performance degradation due to the surface reconstruction during OER. Herein, we found that the incorporation of Ag single atoms in $NiSe_2$ electrocatalyst (Ag_{SA}-$NiSe_2$) could suppress the surface reconstruction, improving both catalytic activity (179 mV@10 mA cm^{-2}) and stability (500 h @ ~100 mA cm^{-2}) for OER in 1.0 M KOH. The aberration corrected transmission electron microscope and X-ray absorption structure analysis reveal the co-existence of the Ag single atoms and Se vacancies in $NiSe_2$ matrix. In-situ Raman spectroscopy demonstrates that the introduction of single-atom Ag and Se vacancies in $NiSe_2$ successfully inhibits the formation of NiOOH species on the surface during OER, accounting for the excellent stability. The theoretical calculation result indicates that the Ag single atom and Se vacancies in $NiSe_2$ synergistically optimizes the adsorption/desorption of OER intermediates, boosting the intrinsic activity.

1. Introduction

Electrochemical water splitting is considered to be one of the most promising routes for hydrogen production because it can be effectively coupling with renewable energy sources such as wind, solar and tidal energy [1–3] However, the anodic oxygen evolution reaction (OER) is a bottleneck in the development of hydrogen production efficiency due to its complex four-electron pathway. [4,5] Currently, the most efficient catalysts for accelerating OER kinetics are noble metal-based materials such as RuO_2 and IrO_2, but the use of noble metal catalysts greatly weakens the cost competitiveness of water electrolysis and hinders its large-scale industrial application. [6,7] The search for non/low noble metal-based catalysts instead of expensive RuO_2 and IrO_2 is highly demanded.

To date, a large number of 3d transition-metal (TM) oxides [8–10], sulfides [11–13], selenides [14] and phosphides [15,16] for OER have been extensively studied. Among these catalysts, transition-metal selenides (TMSe) stand out due to their excellent catalytic activities towards OER, attracting the widespread attention. [17] However, recent studies reveal that TMSe catalysts will undergo the surface oxidation and reconstruction of TMSe under high anodic potential, leading to the partial/whole transformation to amorphous transition-metal oxyhydroxides (TMOOH), and TMOOH is considered as the actual active species rather than TMSe. Moreover, the adsorbed anionic SeO_3^{2-} or SeO_4^{2-} generated during OER on TMOOH will also promote the OER activities, which has been demonstrated by Zhang's group. [18] The aforementioned studies indicate that TMSe catalysts are only precursor template rather than the actually active phase for OER, and much factors such as anions (SeO_3^{2-} or SeO_4^{2-}) and hydroxides/selenides heterointerface will play an important role in influencing the OER activity, making it difficult to reveal the structure-activity relationship. [19–21] Even worse, the surface reconstruction of TMSe will give rise to the dissolution of active metal species, and the generated amorphous TMOOH is also unstable, both of which will lead to the poor stability of this kind of

---

* Corresponding authors at: Key Laboratory of Special Functional Materials for Ecological Environment and Information (Ministry of Education), Hebei University of Technology, Tianjin 300130, PR China.
E-mail addresses: lisj@hebut.edu.cn (S. Li), liuhui2013@hebut.edu.cn (H. Liu).
[1] These authors contributed equally

catalysts. Therefore, inhibiting the surface reconstruction of TMSe is not only beneficial for uncovering the structure-activity relationship, but also good for the catalytic stability. However, it's still a great challenge to suppress the surface reconstruction of TMSe during OER. [11]

Here, we found that incorporating single-atom Ag into $NiSe_2$ (Ag_{SA}-$NiSe_2$) could successfully inhibit the surface construction of the catalyst during OER, which had been validated by a range of in/ex situ characterization techniques. The Ag_{SA}-$NiSe_2$ catalyst exhibits an excellent OER activity in 1.0 M KOH electrolyte, only requiring an ultralow overpotential of 179 mV at a current density of 10 mA cm^{-2}. Inspiringly, the OER activity of the as-obtained single-atom catalyst only decays by about 8% after 500 h long-term durability test at a high current density of $\sim$ 100 mA cm^{-2}, which is obviously better than the pristine $NiSe_2$ that decays by 74.8% after only 100 h stability test. To our best knowledge, the excellent OER performance of the Ag_{SA}-$NiSe_2$ catalyst in terms of activity and stability is among the advanced OER catalysts reported recently. Additionally, in-situ Raman spectroscopy and high-resolution transmission electron microscope (HRTEM) validate that Ag_{SA}-$NiSe_2$ will not be transformed into NiOOH during OER, which is very different from the pristine $NiSe_2$ that is easy to undergo a surface reconstruction to generate amorphous NiOOH. X-ray absorption fine structure (XAFS) and density functional theory (DFT) calculation suggests that the introduction of Ag single atom that occupies Ni site in $NiSe_2$ will strengthen Ni-Se bond, which may be responsible for the inhibition of the surface reconstruction of selenides during OER. Moreover, the boosted intrinsic activity for Ag_{SA}-$NiSe_2$ is mainly attributed to the reduced reaction kinetics barrier (0.64 eV) relative to $NiSe_2$ (0.76 eV).

2. Experimental section

2.1. Materials

$Ni(NO_3)_2$, NH_4F, urea, KOH, $AgNO_3$ and $NaHB_4$ were brought from Aladdin Reagent. Deionized water (DIW) from a Millipore System (Millipore Q) purification system is used to prepare all aqueous solutions.

2.2. Materials synthesis

2.2.1. Synthesis of Ni(OH)₂

0.647 g of $Ni(NO_3)_2$, 0.148 g of NH_4F and 0.6 g of urea were completely dissolved in 35 mL of DIW. The above solutions were then transferred to the autoclave liner where a piece of pre-treated carbon cloth (1×1cm^2) was placed. $Ni(OH)_2$ was obtained after 120 ℃ heating for 6 h, washed and dried.

2.2.2. Synthesis of NiSe₂

$Ni(OH)_2$ was placed at downstream and 0.3 g of Se powder was placed at upstream in a tube furnace. Then it was calcined at 400 °C for 1 h under Ar atmosphere to obtain $NiSe_2$.

2.2.3. Synthesis of Ag₅ₐ-NiSe₂

First, 0.01 g $AgNO_3$ was dissolved in 40 mL of DIW. Then, add $NiSe_2$ into the solution, stir it for 5 min and then add 0.05 g $NaHB_4$, continue to stir for 10 min. Finally, remove obtained Ag_{SA}-$NiSe_2$, wash and dry. The actual loading of Ag single atom is 0.73 wt%.

2.3. Characterization

Used transmission electron microscope (TEM, JEOL-2100 F) and scanning electron microscope (SEM, TESCAN GAIA3GA) to observe the morphology and element composition of the sample. X-ray photoelectron spectrometer made by Thermo Fisher-VG Scientific (ESCALAB 250Xi) was used to analysis the surface chemical state of the samples. The physical phase of the samples (Cu Kα, 4 kW) was determined by
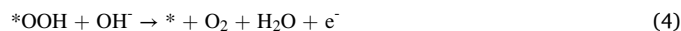
Bruker D8 XRD. Spherical aberration corrected high angle annular dark field images (AC-HAADF-STEM) were acquired on JEOL JEM-ARM300F Grand ARM transmission electrons. Hard XAS of Ag K, Ni K and Se K edges were measured on QAS 7-BM at Brookhaven National Laboratory.

2.4. Electrochemical measurements methods

All electrochemical performance tests in this work were carried out on Chenhua CHI604E electrochemical workstation unless otherwise stated. 1 M KOH solution was used as the electrolyte. A three-electrode system was used: the working electrode was the prepared Ag_{SA}-$NiSe_2$, $NiSe_2$ and other catalysts were, the counter electrode was graphite rod, and the reference electrode was Hg/HgO electrode. A reversible hydrogen electrode (RHE) was used to calibrate all the potentials: $E_{RHE}=E_{Hg/HgO}+0.0592$ pH$+0.095$. Prior to testing using linear scanning voltammetry (LSV), the working electrode was scanned several times over the working potential range by cyclic voltammetry (CV) to activate the working electrode and remove the oxide layer. LSV curves were tested over the range 0–0.8 V at a scan rate of 2 mV s^{-1}. CV tests at different scan rates (0.025–0.1 V s^{-1}) were used to evaluate the double layer capacitance (C_{dl}) over the range 0–0.8 V. The electrochemical surface area (ECSA) of the catalysts was evaluated by C_{dl}. Electrochemical impedance spectroscopy (EIS) measurements were conducted at 1.38 V and frequency scan range was 1 MHz to 10 MHz. The long-term durability of electrocatalysts were assessed by chronoamperometry.

2.5. DFT Calculations

Electronic and structural optimization were performed using density functional theory (DFT) calculations via the Vienna ab-initio Simulation Package (VASP). The GGA-PBE functional is employed to treat the exchange and correlation interactions of electrons, and the PAW method was adapted to represent the ionic cores. A plane wave basis with an energy cutoff of 450 eV was used in all calculations. The following four steps are the OER process:

$$* + OH^- \rightarrow *OH + e^- \tag{1}$$

$$*OH + OH^- \rightarrow *O + H_2O + e^- \tag{2}$$

$$*O + OH^- \rightarrow *OOH + e^- \tag{3}$$

$$*OOH + OH^- \rightarrow * + O_2 + H_2O + e^- \tag{4}$$

The free energy changes of OER process can be calculated with CHE model as follows:

$$\Delta G = \Delta E(ad) + \Delta ZPE - T\Delta S$$

here 'ad' represents the intermediate of adsorption. $\Delta E(ad)$ is the adsorption energy of ad. ΔZPE (ad) is the change of the zero-point energy calculated from the vibration frequency of ad. $\Delta S(ad)$ is the difference between the adsorbed and states entropy (the molecular entropy is taken from the standard value). T is room temperature.

3. Results and discussion

3.1. Structural characterization of materials

Fig. 1a shows the synthetic process of Ag_{SA}-$NiSe_2$ on carbon cloth (Ag_{SA}-$NiSe_2$). The $Ni(OH)_2$ nanoarrays (Figure S1) were first fabricated by a hydrothermal method, followed by vapor phase selenization to form $NiSe_2$. Finally, Ag single atoms were deposited on $NiSe_2$ by chemical reduction. XRD patterns (Fig. 1b) show that Ag_{SA}-$NiSe_2$ has the same pyrite structure as $NiSe_2$ (PDF#41–1495), and no diffraction peaks of Ag nanoparticles are observed, implying that the loaded Ag is in a considerably small size or a relatively small amount on $NiSe_2$ support.
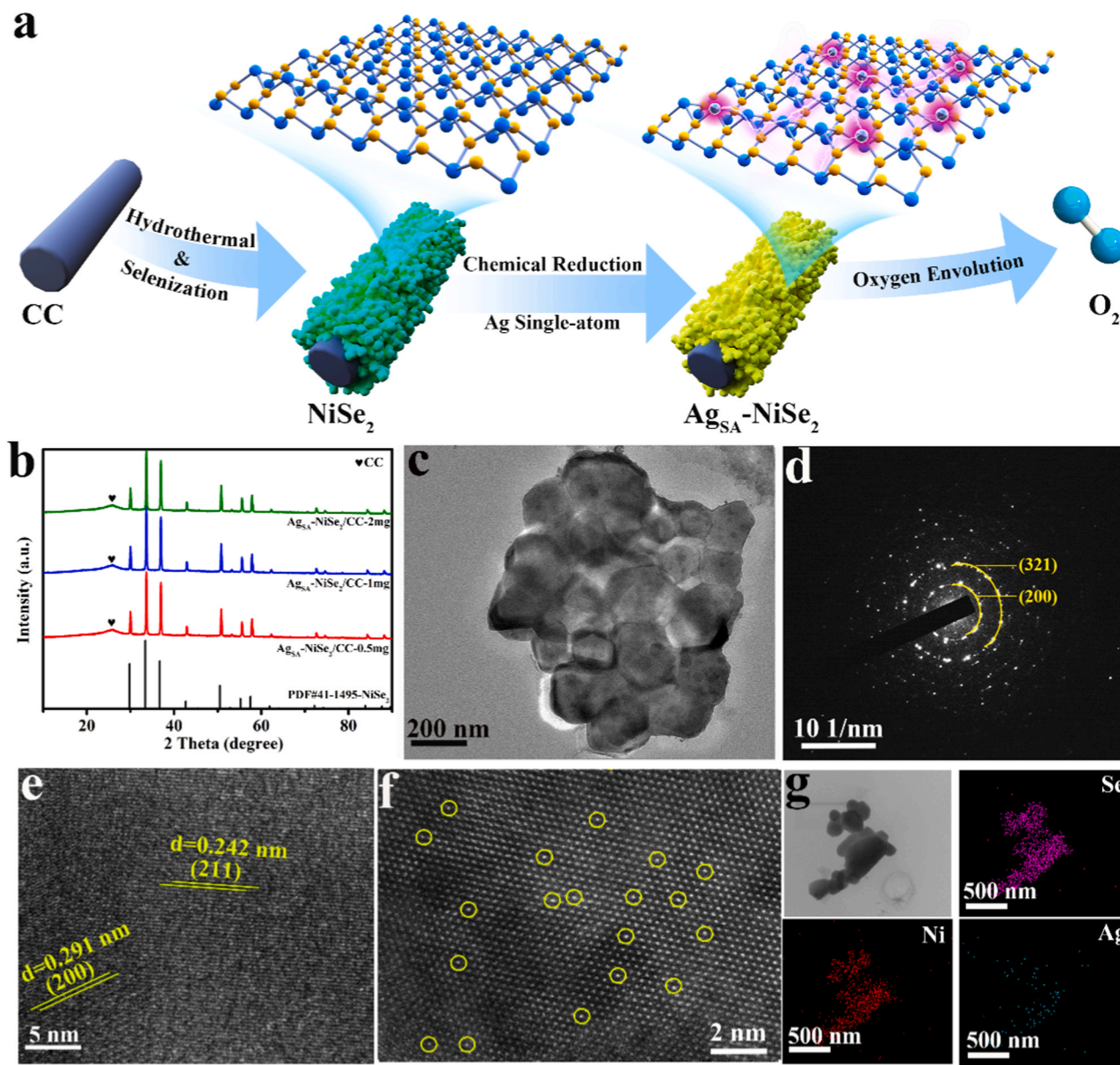
Fig. 1. (a) Illustration for the synthesis of Ag_{SA}-$NiSe_2$. (b) XRD pattern of Ag_{SA}-$NiSe_2$. (c) TEM, (d) SAED, (e) HRTEM, (f) AC-HAADF-STEM image and (g) Element mapping of Ag_{SA}-$NiSe_2$.

[22–24] SEM image shows that $NiSe_2$ catalysts exhibit coral-like nanosheets composed of nanoparticles on carbon cloth (Supplementary Figure S2). Moreover, the morphology of Ag_{SA}-$NiSe_2$ is consistent with that of $NiSe_2$, also suggesting that Ag atoms may be incorporated into the lattice of $NiSe_2$ (Figure S3). TEM images further confirmed that the Ag-$NiSe_2$ nanosheets are consisted of multiple nanoparticles (Fig. 1c). Selected area electron diffraction (SAED) and HRTEM showed the presence of (321), (200) and (211) crystal faces belonging to pyrite Ag_{SA}-$NiSe_2$ (Fig. 1d-e).

AC-HAADF-STEM (Fig. 1f) was used to determine the existing form of Ag. It can be clearly observed that Ag atoms with distinguishable bright spots are uniformly distributed on the lattice of $NiSe_2$ without any obvious nanoparticles or clusters. The above results demonstrate that the incorporated Ag atoms exist in the lattice of $NiSe_2$ in the form of single atoms, which is consistent with the conclusion of XRD. Moreover, the loading amount of Ag in Ag_{SA}-$NiSe_2$ was calculated as 0.73 wt% according to inductively coupled plasma-mass spectrometry (ICP-MS) analysis (Table S1). Elemental mapping of Ni, Se and Ag elements also indicates that Ag atoms are uniformly distributed over the entire $NiSe_2$ without any aggregation (Fig. 1g).

To further identify the chemical state of the catalyst and the coordination configuration of the Ag_{SA}-$NiSe_2$ catalyst, XPS and XAFS spectroscopy were performed. [25,26] The XPS spectrum of Ag_{SA}-$NiSe_2$ confirmed the presence of Ni, Se, and Ag (Figure S4). Fig. 2a shows the Ni 2p spectra of Ag_{SA}-$NiSe_2$ and $NiSe_2$. Ag_{SA}-$NiSe_2$ shows two characteristic peaks at 853.6 and 855.6 eV corresponding to Ni^{2+} and Ni^{3+}, respectively. [27] Compared with the Ni 2p peak of $NiSe_2$, the Ni 2p peak of Ag_{SA}-$NiSe_2$ is slightly shifted to higher binding energy, implying a higher oxidation state. The peaks at 54.9 eV and 55.7 eV in the Se 3d spectrum of Ag_{SA}-$NiSe_2$ in Fig. 2b are associated with the Se $3d_{5/2}$ and Se $3d_{3/2}$ states, respectively. The Se 3d binding energy of Ag_{SA}-$NiSe_2$ is higher compared to $NiSe_2$, indicating that Se in Ag_{SA}-$NiSe_2$ has a higher oxidation state. The weak peak at 58.9 eV is a Se-O peak due to the unavoidable partial oxidation of surface Se. [28] Interestingly, the Ag-Se bond (53.9 eV) appears in the XPS spectrum of Se 3d of Ag_{SA}-$NiSe_2$, proving the existence of Ag-Se coordination.
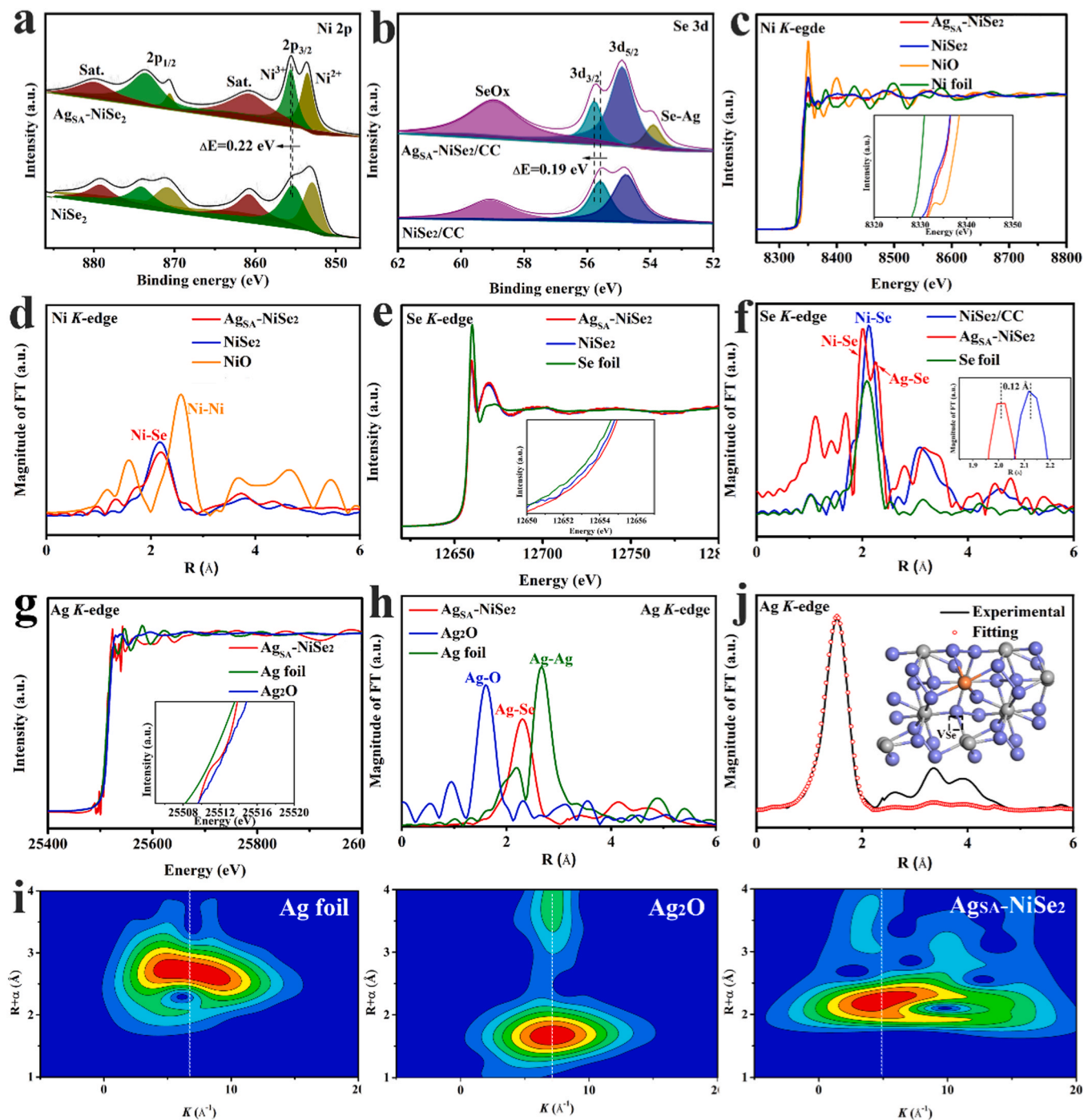
Fig. 2. (a) XPS spectra for Ni 2p of NiSe$_2$ and Ag$_{SA}$-NiSe$_2$. (b) XPS spectra for Se 3d of NiSe$_2$ and Ag$_{SA}$-NiSe$_2$. (c) The Ni K-edge XAFS spectra. (d) R-space Ni *K*-edge EXAFS spectra of Ag$_{SA}$-NiSe$_2$. NiSe$_2$, Ni foil and NiO as references. (e) The Se *K*-edge XAFS spectra. (f) R-space Se *K*-edge EXAFS spectra of Ag$_{SA}$-NiSe$_2$. NiSe$_2$ and Se foil as references. (g) The experimental Ag *K*-edge XAFS spectra. (h) R-space Ag *K*-edge EXAFS spectra of Ag$_{SA}$-NiSe$_2$. Ag$_2$O and Ag foil as references. (i) WT-EXAFS plots of Ag foil, Ag$_2$O and Ag$_{SA}$-NiSe$_2$, respectively. (j) FT-EXAFS fitting curves of Ag$_{SA}$-NiSe$_2$ at Ag *K*-edge. (inset: Schematic model of Ag$_{SA}$-NiSe$_2$. Gray: Ni, blue: Se, Orange: Ag).

Further investigation of the overall chemical state and fine coordination structure of Ag$_{SA}$-NiSe$_2$ and NiSe$_2$ catalysts were investigated by XAFS. For *K*-edge, the absorption edge of Ni in Ag$_{SA}$-NiSe$_2$ shifts towards higher energy compared to NiSe$_2$ (Fig. 2c), suggesting that Ni presents a higher valence state after the introduction of Ag, which is consistent with the XPS analysis. [29] Fourier transformed extended X-ray absorption fine structure (EXAFS) spectroscopy is used to resolve the local coordination structure. The intensity of the main peak (~2.16 Å) in the EXAFS spectrum of the Ag$_{SA}$-NiSe$_2$ Ni K-edge is significantly lower than

that of pristine NiSe$_2$ (Fig. 2d), which suggests that the Ni-Se coordination numbers in Ag$_{SA}$-NiSe$_2$ is reduced. To obtain the specific Ni-Se coordination numbers, the Ni *K*-edge EXAFS of Ag$_{SA}$-NiSe$_2$ and NiSe$_2$ were fitted. The results are shown in Figure S5-S6 and Table S2, where the Ni-Se coordination numbers in NiSe$_2$ are about 6, while that in Ag$_{SA}$-NiSe$_2$ are about 5, implying that Se vacancies are generated after incorporating Ag atoms. Electron paramagnetic resonance (EPR) result also validates the existence of Se vacancies (Figure S7). [30] The oxidation state of Se in Ag$_{SA}$-NiSe$_2$ is higher than that of Se in NiSe$_2$

(Fig. 2e), which is consistent with the XPS results of Se 3d. In Fig. 2f, it is obvious that the main peak in Ag$_{SA}$-NiSe$_2$ that belongs to Ni-Se coordination is splitting into two peaks, which are assigned to Ni-Se bond (2.00 Å) and Ag-Se bond (2.22 Å), respectively, agreeing well with the XPS spectrum of Se 3d (Fig. 2d). The above analysis shows that Ag may occupy the Ni sites in NiSe$_2$ and coordinate with Se. Further, from the enlarged image in Fig. 2f, the Ni-Se bond length in Ag$_{SA}$-NiSe$_2$ (2.00 Å) is obviously shorter than that in the original NiSe$_2$ (2.13 Å), suggesting that the introduction of Ag strengthens the bond between Ni and Se in NiSe$_2$, which may be beneficial to the structure stability of NiSe$_2$. [31, 32]

Fig. 2g shows the XANES spectra of Ag K-edge in Ag$_{SA}$-NiSe$_2$, Ag foil and Ag$_2$O. The absorption edge of Ag$_{SA}$-NiSe$_2$ is located between Ag$_2$O and Ag foil, indicating that the valence state of Ag lies between 0 and +2. [33,34] The fitting result indicate that the oxidation state of Ag in Ag$_{SA}$-NiSe$_2$ is about +0.53 (Figure S8). In addition, no Ag-Ag bond was observed in the EXAFS spectrum of Ag$_{SA}$-NiSe$_2$ (Fig. 2h), proving that Ag exists as single atom [35,36], which in agreement with the results of the AC-HADDF-STEM. The maximum peak of Ag K-edge Wavelet Transform (WT)-EXAFS is at 4.97 Å^{-1}, while the maximum peaks of Ag$_2$O and Ag foil are located at 6.97 Å^{-1} and 5.98 Å^{-1}. further demonstrating the atomic dispersion of Ag in Ag$_{SA}$-NiSe$_2$ (Fig. 2i). The fitted EXAFS curves for Ag$_{SA}$-NiSe$_2$ are shown in Fig. 2j and the corresponding parameters are listed in Table S2, suggesting that Ag atoms occupy Ni sites in NiSe$_2$.

The coordination number of Ag-Se bond is 5, demonstrating the existence of Se vacancies around Ag, which is consistent with the EPR result.

3.2. Electrocatalytic OER performance

The electrocatalytic performances towards OER were tested in 1.0 M KOH by using a standard three-electrode system. LSV curves (Fig. 3a) were used to assess the OER activity of individual catalysts. Compared to pristine NiSe$_2$ (327 mV), Ni(OH)$_2$ (375 mV) and commercial IrO$_2$ (328 mV), Ag$_{SA}$-NiSe$_2$ showed excellent OER activity, requiring only ultra-low overpotential of 179 mV to achieve 10 mA cm^{-2} current density. The Tafel slope obtained from the LSV polarization curve is shown in Fig. 3b. Ag$_{SA}$-NiSe$_2$ (60.0 mV dec^{-1}) has the lowest Tafel slope value compared with NiSe$_2$ (105.8 mV dec^{-1}) and commercial IrO$_2$ (62.7 mV dec^{-1}), suggesting Ag$_{SA}$-NiSe$_2$ has significantly enhanced OER kinetics. Compared with other recently reported transition metal chalcogenides catalysts, the as-prepared Ag$_{SA}$-NiSe$_2$ in this work shows better catalytic activity (Fig. 3c and Table S3) [19,37–48], which is identified as one of the state-of-the-art OER catalysts. Due to the positive correlation between C$_{dl}$ and ECSA, the ECSA of the electrocatalyst can be calculated by C$_{dl}$. Comparing with NiSe$_2$ (2 mF cm^{-2}), Ag$_{SA}$-NiSe$_2$ (19.5 mF cm^{-2}) has a much higher C$_{dl}$ value (Fig. 3d), suggesting more electrocatalytically active sites for Ag$_{SA}$-NiSe$_2$. The ECSA-normalized LSV curves of Ag$_{SA}$-NiSe$_2$ and NiSe$_2$ (Figure S9) demonstrate that the
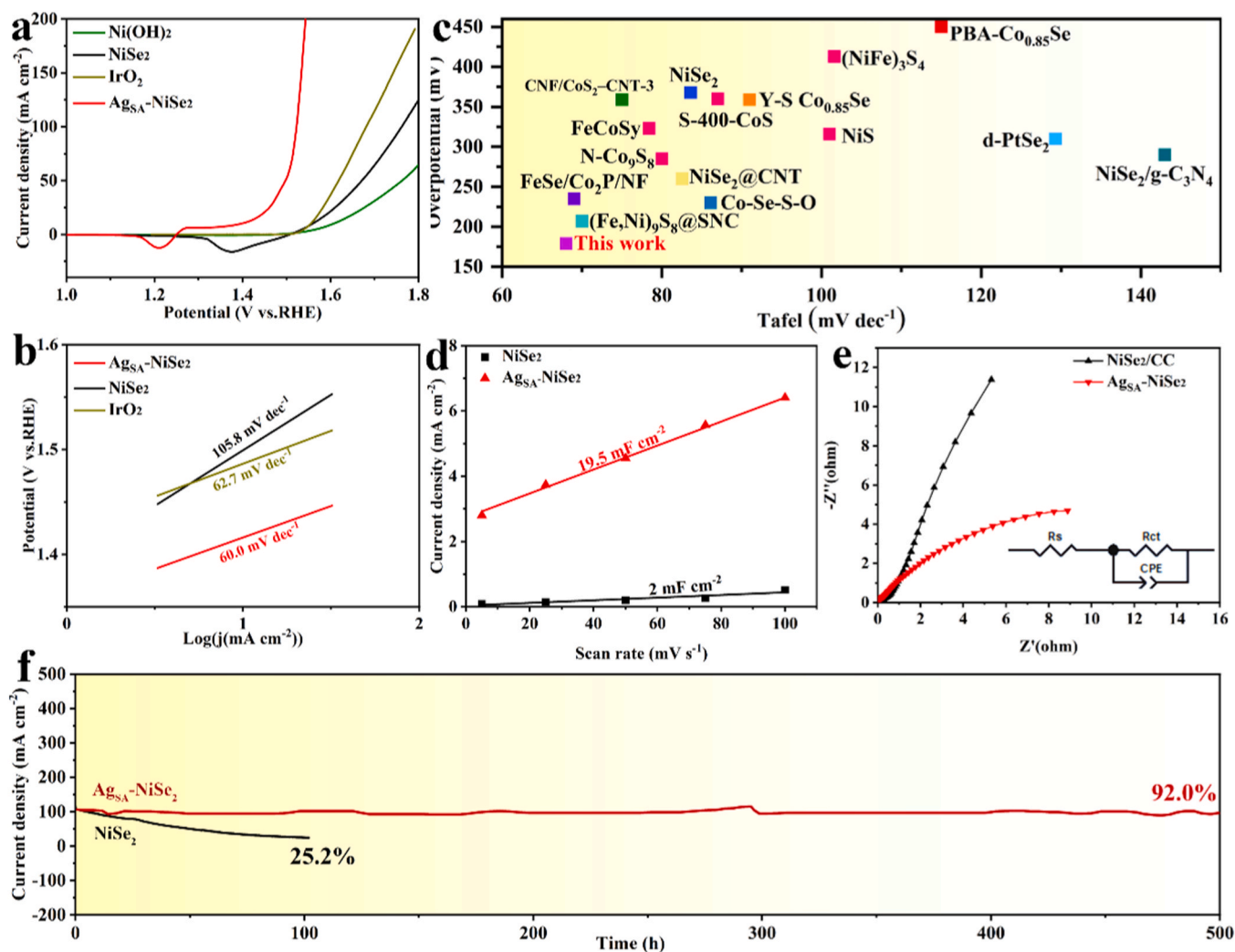
Fig. 3. Electrocatalytic performance of the NiSe$_2$, Ag$_{SA}$-NiSe$_2$, Ni(OH)$_2$ and IrO$_2$ for OER in 1.0 M KOH electrolyte. (a) LSV. (b) Tafel. (c) Compared with other recently reported transition metal chalcogenides catalysts at 10 mA cm^{-2} in 1.0 M KOH. (d) C$_{dl}$. (e) EIS. (f) Chronoamperometry curve of NiSe$_2$ and Ag$_{SA}$-NiSe$_2$.

intrinsic activity of Ag$_{SA}$-NiSe$_2$ is still superior to that of NiSe$_2$. The charge transfer characteristics of Ag$_{SA}$-NiSe$_2$ were analyzed using EIS. The results (Fig. 3d) show that the R$_{ct}$ value of Ag$_{SA}$-NiSe$_2$ ($\approx$ 17.9 Ω) is much lower than that of NiSe$_2$ ($\approx$ 20.1 Ω), suggesting a fast electron transfer rate at the solid-liquid interface. The stability of the catalyst is also a key parameter for evaluating the performance of OER in practical applications. We evaluated the stability of Ag$_{SA}$-NiSe$_2$ using the chronoamperometry (Fig. 3f). Surprisingly, Ag$_{SA}$-NiSe$_2$ worked for 500 h at a high current density of about 100 mA cm^{-2} with only 8% degradation, which is obviously superior to NiSe$_2$ that exhibits 74.8% degradation and another advanced transition metal chalcogenides catalysis (Table S4). This validates the ability of Ag$_{SA}$-NiSe$_2$ for industrial applications.

3.3. Structure evolution of materials

Previous researches have noted that selenides are undergoing seriously superficial oxidation and reconstruction during OER process. [18,49,50] To investigate the surface reconstruction, in-situ Raman testing was carried out. Fig. 4a shows the in-situ Raman data of NiSe$_2$, at the potential of OCV, a small broad peak at 400–600 cm^{-1} belong to amorphous NiOOH. This proves that amorphous NiOOH layer is formed on the surface of NiSe$_2$ in alkaline electrolyte even without applying a positive voltage, indicating that the pristine NiSe$_2$ is very unstable. With the increase of anodic potential, the characteristic peaks (400–600 cm^{-1}) belonged to amorphous NiOOH in the NiSe$_2$ samples were gradually enhanced, [51–53] while no NiOOH phase can be observed in Ag$_{SA}$-NiSe$_2$ sample (Fig. 4b), indicating that the introduction of Ag may effectively inhibit the structural transformation of NiSe$_2$. Similarly, the TEM results showed that that an amorphous layer with a thickness of about 50 nm forms on the pristine NiSe$_2$ after stability testing (Figs. 4c and 4d), the amorphous ring shown by SAED also proves this point (the inset of Fig. 4c). While no amorphous layer was observed on the Ag$_{SA}$-NiSe$_2$ surface (Fig. 4e and f), SAED also shows

clear polycrystalline rings corresponding to the (220) and (200) crystal plane (the inset of Fig. 4e), which was consistent with the in-situ Raman results. Moreover, according to the EDS results (Table S5), Se/Ni ratio in NiSe$_2$ decreased from 1.21 to 0.64 before and after the stability test, indicating that a serious loss of Se in NiSe$_2$, whereas the Se/Ni ratio in Ag$_{SA}$-NiSe$_2$ did not change much before and after the stability test.

The XPS results of the samples after stability testing (Figure S10) also indicate that the introduction of Ag single atom greatly inhibits the superficial oxidation and reconstruction of NiSe$_2$ during OER. Meanwhile, the XRD and SEM results of Ag$_{SA}$-NiSe$_2$ after stability test also remained unchanged compared with the pristine Ag$_{SA}$-NiSe$_2$ (Figure S11a,b). Moreover, the AC-HAADF-STEM image shows that the single-atom Ag atoms (bright spots) are uniformly distributed on the substrate surface without obvious aggregation and loss (Figure S11c). The ICP-MS results after the stability test also showed that the loading of Ag single atoms (0.69 wt%) remained almost unchanged compared to the pre-test (0.73 wt%). The obtained EDS mapping image shows that Ag, Ni, Se and O are still uniformly distributed on the whole Ag$_{SA}$-NiSe$_2$ sample (Figure S11d). The signal of Ag in XPS was clearly visible (Figure S12). In general, the introduction of single-atom Ag into NiSe$_2$ can inhibit the superficial oxidation and prevent the phase transformation from NiSe$_2$ to NiOOH, which not only benefit the enhanced catalytic activity, but also is good for stability.

3.4. DFT calculation revealed synergistic effect

DFT calculations were further performed to elucidate the effect of Ag single atom on the catalytic performance of NiSe$_2$. According to the EXAFS fitting results and the structural characterization after stability, the model of Ag$_{SA}$-NiSe$_2$ with Se vacancies was constructed (Figure S13), and the model of NiSe$_2$ was also constructed as a control sample. The reaction pathway for alkaline OER consists of four steps accompanied by the formation of a series of intermediates (*OH, *O, and *OOH). [54,55] The OER pathway maps (Ni is the active site) of Ag$_{SA}$-NiSe$_2$ and NiSe$_2$
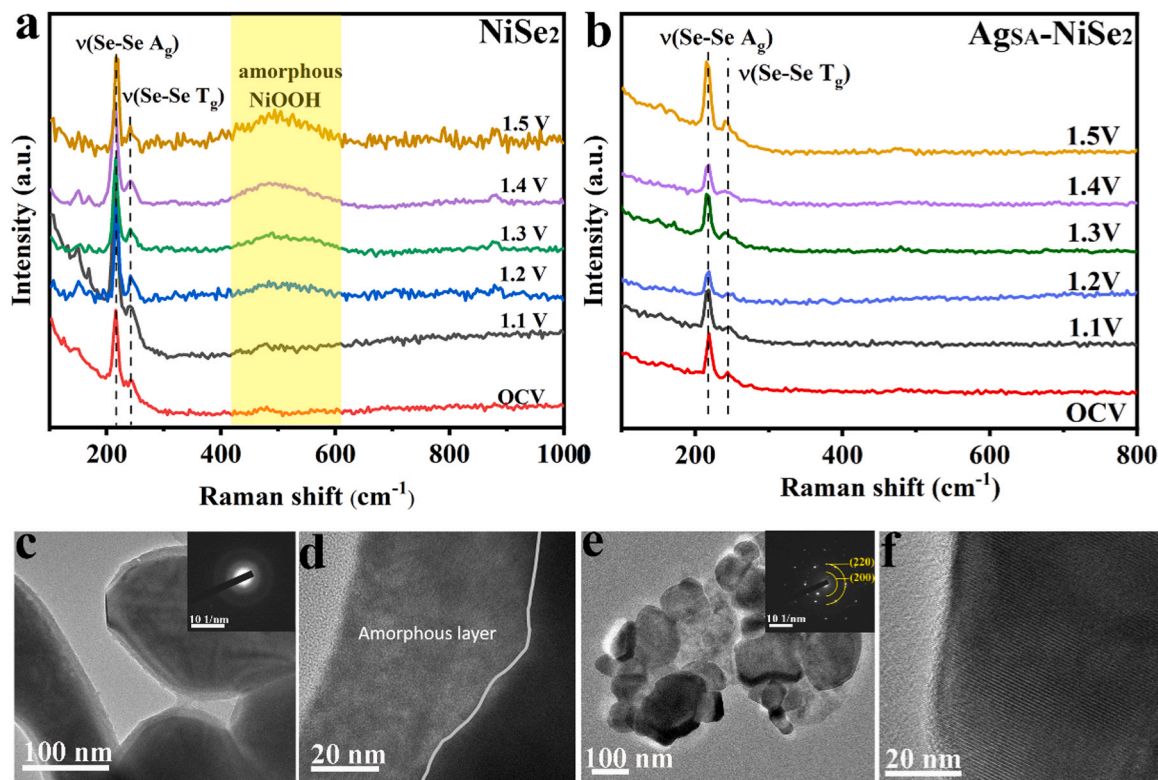

Fig. 4. In situ Raman spectra recorded by (a) NiSe$_2$ and (b) Ag$_{SA}$-NiSe$_2$ in the potential range of 1.1–1.5 V vs. RHE. (c) TEM (inset is the SAED pattern) and (d) HRTEM of NiSe$_2$ after stability test. (e) TEM (inset is the SAED pattern) and (f) HRTEM of Ag$_{SA}$-NiSe$_2$ after stability test.

are shown in Fig. 5a. In NiSe$_2$, the rate-determining step is from *OH to *O, with an overpotential of 0.76 V. Unlike NiSe$_2$, the rate-determining step of Ag$_{SA}$-NiSe$_2$ is from *O to *OOH, with a lower overpotential of 0.64 V, implying a boosted intrinsic activity. Compared with NiSe$_2$, Ag$_{SA}$-NiSe$_2$ exhibits more electronic states densities near the Fermi level, indicating that the conductivity of Ag$_{SA}$-NiSe$_2$ electronic structure is better than NiSe$_2$ (Fig. 5b). Moreover, it is worth noting that the introduction of Ag single atom and Se vacancies causes the d-band center of NiSe$_2$ to approach the Fermi level, implying the strengthening of the bonding between the oxygen-containing intermediates and the active sites according to d-band center theory raised by Norskov, which is conducive to the OER. [56] The crystal orbital Hamiltonian population (COHP), as illustrated in Fig. 5c, further supports this by examining the interaction between the *O intermediate and the active center Ni. Positive -COHP often indicates bonding contributions, whereas negative -COHP generally indicates antibonding contributions. [57,58] Based on the quantitative integrated COHP (ICOHP) that reflects quantitative bonding contributions, a more negative ICOHP value of −2.72344 eV in Ag$_{SA}$-NiSe$_2$ than that in NiSe$_2$ (−2.37301 eV) implies a stronger bonding between Ni site and O intermediate in Ag$_{SA}$-NiSe$_2$.

To gain a deep insight into the good stability of Ag$_{SA}$-NiSe$_2$, the formation energies of Ag$_{SA}$-NiSe$_2$ and NiSe$_2$ were calculated, as shown in Figure S14. The formation energy of Ag$_{SA}$-NiSe$_2$ (−21.32 eV) is lower than that of NiSe$_2$ (−20.11 eV), indicating that Ag$_{SA}$-NiSe$_2$ is more stable than NiSe$_2$ in terms of thermodynamics. [22,59] Further, the COHP result (Fig. 5d) shows that the Ni-Se bond in Ag$_{SA}$-NiSe$_2$ (ICOHP = −2.51965 eV) is much stronger than that in NiSe$_2$ (ICOHP = −1.76613 eV), [60] which may explain the fact that Ag$_{SA}$-NiSe$_2$ can be avoid of the superficial oxidation and phase transformation during OER.

To further reveal the synergistic effect between Ag single atoms and Se vacancies in Ag$_{SA}$-NiSe$_2$ from the atomic scale, we calculated the OER pathway energy diagrams of Ag$_{SA}$-NiSe$_2$ without Se vacancy and NiSe$_2$ with Se vacancy (NiSe$_2$-V$_{Se}$), respectively, as shown in Figure S15-S16. The overpotential of Ag$_{SA}$-NiSe$_2$ without Se vacancies and NiSe$_2$-V$_{Se}$ are 0.72 V and 0.74 V, respectively, which are smaller than that of NiSe$_2$ (0.76 V), but larger than that of Ag$_{SA}$-NiSe$_2$ containing Se vacancy (0.64 V) (Fig. 5a). This suggests that Se vacancies and Ag single atoms synergistically strengthen the intrinsic activity of NiSe$_2$. The COHP (Figure S17) of Ag$_{SA}$-NiSe$_2$ without Se vacancies was further calculated for evaluating the Ni-Se bonding strength, and ICOHP value is more positive compared with that of Ag$_{SA}$-NiSe$_2$ with Se vacancies, which implies weaker Ni-Se bond. The above analysis further confirms the synergistic effect of Ag single atoms and Se vacancies in enhancing the activity and stability of NiSe$_2$.

4. Conclusions

In summary, we reported a novel NiSe$_2$ electrocatalyst decorated with Ag single atoms and Se vacancies (Ag$_{SA}$-NiSe$_2$), which not only exhibits high catalytic activity towards alkaline OER (179 mV@ 10 mA cm^{-2}), but also displays excellent long-terms stability up to 500 h. The experimental and theoretical results validate that the incorporation of Ag single atoms and Se vacancies synergistically optimize the electronic configuration of NiSe$_2$, lowering the energy barrier of OER process and boosting the intrinsic activity. But more importantly, the obviously strengthened Ni-Se bond in Ag$_{SA}$-NiSe$_2$ successfully inhabit the superficial oxidation and reconstruction, boosting the catalytic stability, which is very different from the conventional NiSe$_2$ that will undergo a surface reconstruction from NiSe$_2$ to NiOOH during alkaline OER. This work opens up new opportunities in designing high-efficient and stable transition-metal chalcogenide electrocatalysts and beyond towards OER.
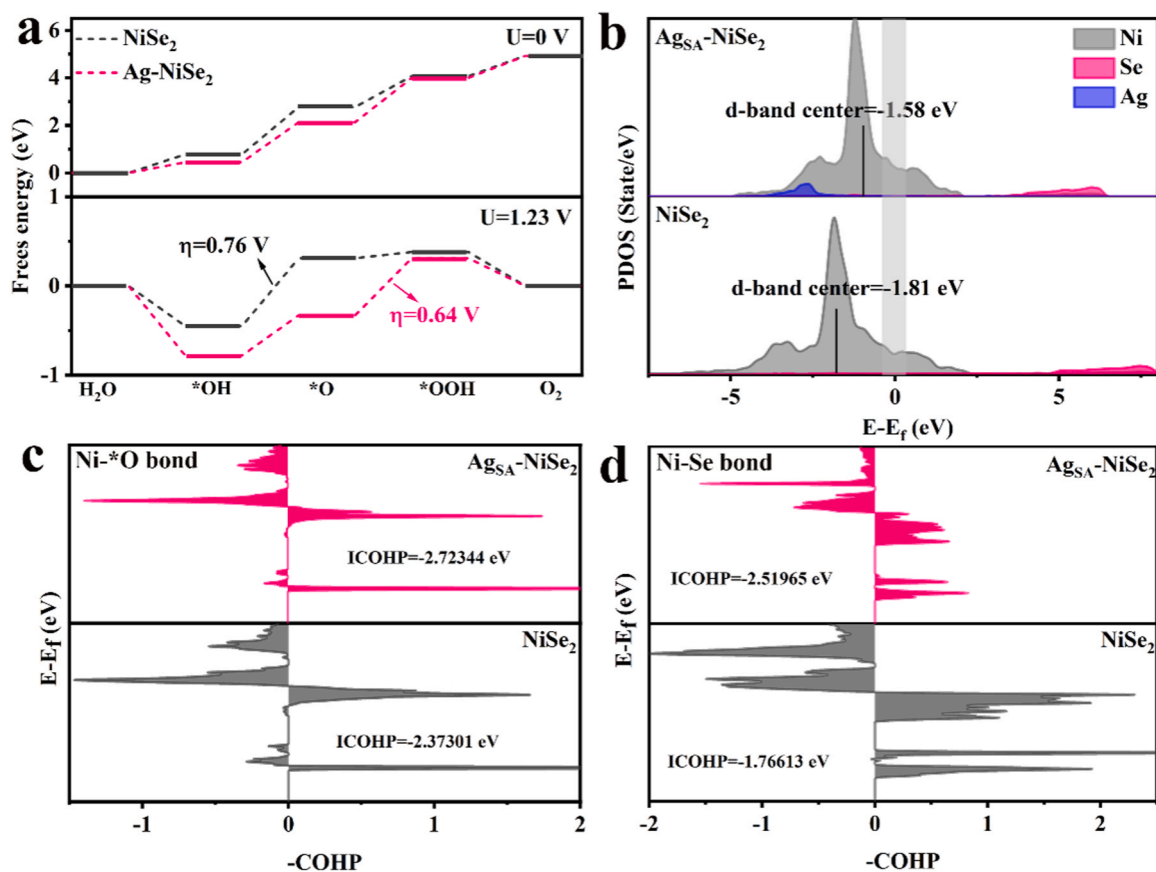

Fig. 5. (a) Free-energy diagram for OER process on NiSe$_2$ and Ag$_{SA}$-NiSe$_2$ at the U=0 V and U=1.23 V. (b) The d-band centers of Ag$_{SA}$-NiSe$_2$ and NiSe$_2$. (c) COHP between chemisorbed *O and Ni site on Ag$_{SA}$-NiSe$_2$ and NiSe$_2$. (d) COHP between Ni and Se atom on Ag$_{SA}$-NiSe$_2$ and NiSe$_2$.

CRediT authorship contribution statement

Liu Hui: Writing – review & editing, Project administration, Funding acquisition. **Li Sijia:** Methodology. **Yuan Wenhao:** Visualization. **Hao Qiuyan:** Funding acquisition. **Sasaki Kotaro:** Resources. **Liang Limin:** Resources. **Li Ying:** Software. **Zhao Xueru:** Resources. **Wang Fangqing:** Writing – original draft, Data curation.

Declaration of Competing Interest

The authors declare that they have no known competing financial interests or personal relationships that could have appeared to influence the work reported in this paper.

Data availability

Data will be made available on request.

Appendix A. Supporting information

Supplementary data associated with this article can be found in the online version at doi:10.1016/j.apcatb.2024.123830.

References

[1] K. Du, L. Zhang, J. Shan, J. Guo, J. Mao, C.-C. Yang, C.-H. Wang, Z. Hu, T. Ling, Interface engineering breaks both stability and activity limits of RuO$_2$ for sustainable water oxidation, Nat. Commun. 13 (2022) 5448.

[2] Z.-F. Huang, J. Song, Y. Du, S. Xi, S. Dou, J.M.V. Nsanzimana, C. Wang, Z.J. Xu, X. Wang, Chemical and structural origin of lattice oxygen oxidation in Co–Zn oxyhydroxide oxygen evolution electrocatalysts, Nat. Energy 4 (2019) 329–338.

[3] G.T.K.K. Gunasooriya, J.K. Nørskov, Analysis of acid-stable and active oxides for the oxygen evolution reaction, ACS Energy Lett. 5 (2020) 3778–3787.

[4] Y. Jiao, Y. Zheng, M. Jaroniec, S.Z. Qiao, Design of electrocatalysts for oxygen- and hydrogen-involving energy conversion reactions, Chem. Soc. Rev. 44 (2015) 2060–2086.

[5] H. Xiao, H. Shin, W.A. Goddard III, Synergy between Fe and Ni in the optimal performance of (Ni, Fe)OOH catalysts for the oxygen evolution reaction, Pnatl. acad. sci. U. S. A. 115 (2018) 5872–5877.

[6] O.J. Guerra, J. Eichman, J. Kurtz, B.-M. Hodge, Cost competitiveness of electrolytic hydrogen, Joule 3 (2019) 2425–2443.

[7] K.A. Stoerzinger, O. Diaz-Morales, M. Kolb, R.R. Rao, R. Frydendal, L. Qiao, X. R. Wang, N.B. Halck, J. Rossmeisl, H.A. Hansen, T. Vegge, I.E.L. Stephens, M.T. M. Koper, Y. Shao-Horn, Orientation-dependent oxygen evolution on RuO$_2$ without lattice exchange, ACS Energy Lett. 2 (2017) 876–881.

[8] F. Song, L. Bai, A. Moysiadou, S. Lee, C. Hu, L. Liardet, X. Hu, Transition metal oxides as electrocatalysts for the oxygen evolution reaction in alkaline solutions: an application-inspired renaissance, J. Am. Chem. Soc. 140 (2018) 7748–7759.

[9] M. Yao, N. Wang, W. Hu, S. Komarneni, Novel hydrothermal electrodeposition to fabricate mesoporous film of Ni$_{0.8}$Fe$_{0.2}$ nanosheets for high performance oxygen evolution reaction, Appl. Catal. B 233 (2018) 226–233.

[10] Y.-Q. Zhang, M. Li, B. Hua, Y. Wang, Y.-F. Sun, J.-L. Luo, A strongly cooperative spinel nanohybrid as an efficient bifunctional oxygen electrocatalyst for oxygen reduction reaction and oxygen evolution reaction, Appl. Catal. B 236 (2018) 413–419.

[11] R. Chen, Z. Zhang, Z. Wang, W. Wu, S. Du, W. Zhu, H. Lv, N. Cheng, Constructing air-stable and reconstruction-inhibited transition metal sulfide catalysts via tailoring electron-deficient distribution for water oxidation, ACS Catal. 12 (2022) 13234–13246.

[12] C. Xuan, W. Lei, J. Wang, T. Zhao, C. Lai, Y. Zhu, Y. Sun, D. Wang, Sea urchin-like Ni–Fe sulfide architectures as efficient electrocatalysts for the oxygen evolution reaction, J. Mater. Chem. A 7 (2019) 12350–12357.

[13] Y. Hu, Y. Zheng, J. Jin, Y. Wang, Y. Peng, J. Yin, W. Shen, Y. Hou, L. Zhu, L. An, M. Lu, P. Xi, C.-H. Yan, Understanding the sulphur-oxygen exchange process of metal sulphides prior to oxygen evolution reaction, Nat. Commun. 14 (2023) 1949.

[14] H. Zhou, F. Yu, Y. Liu, J. Sun, Z. Zhu, R. He, J. Bao, W.A. Goddard, S. Chen, Z. Ren, Outstanding hydrogen evolution reaction catalyzed by porous nickel diselenide electrocatalysts, Energy Environ. Sci. 10 (2017) 1487–1492.

[15] Q. Wang, Z. Liu, H. Zhao, H. Huang, H. Jiao, Y. Du, MOF-derived porous Ni$_2$P nanosheets as novel bifunctional electrocatalysts for the hydrogen and oxygen evolution reactions, J. Mater. Chem. A 6 (2018) 18720–18727.

[16] S. Sun, X. Zhou, B. Cong, W. Hong, G. Chen, Tailoring the d-band centers endows (Ni$_x$Fe$_{1−x}$)$_2$P nanosheets with efficient oxygen evolution catalysis, ACS Catal. 10 (2020) 9086–9097.

[17] Y. Dou, C.-T. He, L. Zhang, H. Yin, M. Al-Mamun, J. Ma, H. Zhao, Approaching the activity limit of CoSe$_2$ for oxygen evolution via Fe doping and Co vacancy, Nat. Commun. 11 (2020) 1664.

[18] Y. Shi, W. Du, W. Zhou, C. Wang, S. Lu, S. Lu, B. Zhang, Unveiling the promotion of surface-adsorbed chalcogenate on the electrocatalytic oxygen evolution reaction, , Angew. Chem. Int. Ed. 59 (2020) 22470–22474.

[19] S. Liu, Y. Xing, Z. Zhou, Y. Yang, Y. Li, X. Xiao, C. Wang, Heterostructure iron selenide/cobalt phosphide films grown on nickel foam for oxygen evolution, J. Mater. Chem. A 11 (2023) 8330–8341.

[20] H. Jia, N. Yao, C. Yu, H. Cong, W. Luo, Unveiling the electrolyte cations dependent kinetics on CoOOH-catalyzed oxygen evolution reaction, Angew. Chem. Inter. Ed. (2023) e202313886.

[21] X. Zhou, X. Liao, X. Pan, M. Yan, L. He, P. Wu, Y. Zhao, W. Luo, L. Mai, Unveiling the role of surface P–O group in P-doped Co$_3$O$_4$ for electrocatalytic oxygen evolution by On-chip micro-device, Nano Energy 83 (2021) 105748.

[22] F.-F. Zhang, C.-Q. Cheng, J.-Q. Wang, L. Shang, Y. Feng, Y. Zhang, J. Mao, Q.-J. Guo, Y.-M. Xie, C.-K. Dong, Y.-H. Cheng, H. Liu, X.-W. Du, Iridium oxide modified with silver single atom for boosting oxygen evolution reaction in acidic media, ACS Energy Lett. 6 (2021) 1588–1595.

[23] X. Mu, X. Gu, S. Dai, J. Chen, Y. Cui, Q. Chen, M. Yu, C. Chen, S. Liu, S. Mu, Breaking the symmetry of single-atom catalysts enables an extremely low energy barrier and high stability for large-current-density water splitting, Energy Environ. Sci. 15 (2022) 4048–4057.

[24] J. Zhang, J. Liu, L. Xi, Y. Yu, N. Chen, S. Sun, W. Wang, K.M. Lange, B. Zhang, Single-atom Au/NiFe layered double hydroxide electrocatalyst: probing the origin of activity for oxygen evolution reaction, J. Am. Chem. Soc. 140 (2018) 3876–3879.

[25] H. Yang, F. Li, S. Zhan, Y. Liu, W. Li, Q. Meng, A. Kravchenko, T. Liu, Y. Yang, Y. Fang, L. Wang, J. Guan, I. Furó, M.S.G. Ahlquist, L. Sun, Intramolecular hydroxyl nucleophilic attack pathway by a polymeric water oxidation catalyst with single cobalt sites, Nat. Catal. 5 (2022) 414–429.

[26] S. Li, B. Chen, Y. Wang, M.-Y. Ye, P.A. van Aken, C. Cheng, A. Thomas, Oxygen-evolving catalytic atoms on metal carbides, Nat. Mater. 20 (2021) 1240–1247.

[27] B.H.R. Suryanto, Y. Wang, R.K. Hocking, W. Adamson, C. Zhao, Overall electrochemical splitting of water at the heterogeneous interface of nickel and iron oxide, Nat. Commun. 10 (2019) 5599.

[28] P. Ge, S. Li, L. Xu, K. Zou, X. Gao, X. Cao, G. Zou, H. Hou, X. Ji, Hierarchical hollow-microsphere metal–selenide@carbon composites with rational surface engineering for advanced sodium storage, Adv. Energy Mater. 9 (2019) 1803035.

[29] M. Favaro, W.S. Drisdell, M.A. Marcus, J.M. Gregoire, E.J. Crumlin, J.A. Haber, J. Yano, An operando investigation of (Ni–Fe–Co–Ce)Ox system as highly efficient electrocatalyst for oxygen evolution reaction, ACS Catal. 7 (2017) 1248–1258.

[30] I.S. Kwon, I.H. Kwak, T.T. Debela, J.Y. Kim, S.J. Yoo, J.-G. Kim, J. Park, H.S. Kang, Phase-transition Mo1−xVxSe2 alloy nanosheets with rich V–Se vacancies and their enhanced catalytic performance of hydrogen evolution reaction, ACS Nano 15 (2021) 14672–14682.

[31] R. Zhang, C. Wang, P. Zou, R. Lin, L. Ma, L. Yin, T. Li, W. Xu, H. Jia, Q. Li, S. Sainio, K. Kisslinger, S.E. Trask, S.N. Ehrlich, Y. Yang, A.M. Kiss, M. Ge, B.J. Polzin, S. J. Lee, W. Xu, Y. Ren, H.L. Xin, Compositionally complex doping for zero-strain zero-cobalt layered cathodes, Nature 610 (2022) 67–73.

[32] P. Zou, L. Yao, C. Wang, S.J. Lee, T. Li, H.L. Xin, Regulating cation interactions for zero-strain and high-voltage P2-type Na$_{2/3}$Li$_{1/6}$Co$_{1/6}$Mn$_{2/3}$O$_2$ layered oxide cathodes of sodium-ion batteries, Angew. Chem. Int. Ed. 62 (2023) e202304628.

[33] H. Shang, X. Zhou, J. Dong, A. Li, X. Zhao, Q. Liu, Y. Lin, J. Pei, Z. Li, Z. Jiang, D. Zhou, L. Zheng, Y. Wang, J. Zhou, Z. Yang, R. Cao, R. Sarangi, T. Sun, X. Yang, X. Zheng, W. Yan, Z. Zhuang, J. Li, W. Chen, D. Wang, J. Zhang, Y. Li, Engineering unsymmetrically coordinated Cu-S$_1$N$_3$ single atom sites with enhanced oxygen reduction activity, Nat. Commun. 11 (2020) 3049.

[34] K. Yuan, D. Lützenkirchen-Hecht, L. Li, L. Shuai, Y. Li, R. Cao, M. Qiu, X. Zhuang, M.K.H. Leung, Y. Chen, U. Scherf, Boosting oxygen reduction of single iron active sites via geometric and electronic engineering: nitrogen and phosphorus dual coordination, J. Am. Chem. Soc. 142 (2020) 2404–2412.

[35] C. Zhu, Q. Shi, S. Feng, D. Du, Y. Lin, Single-atom catalysts for electrochemical water splitting, ACS Energy Lett. 3 (2018) 1713–1721.

[36] P. Vancsó, Z.I. Popov, J. Pető, T. Ollár, G. Dobrik, J.S. Pap, C. Hwang, P.B. Sorokin, L. Tapasztó, Transition metal chalcogenide single layers as an active platform for single-atom catalysis, ACS Energy Lett. 4 (2019) 1947–1953.

[37] Y. Huang, L.-W. Jiang, B.-Y. Shi, K.M. Ryan, J.-J. Wang, Highly efficient oxygen evolution reaction enabled by phosphorus doping of the Fe electronic structure in iron–nickel selenide nanosheets, Adv. Sci. 8 (2021) 2101775.

[38] S. Wang, P. He, L. Jia, M. He, T. Zhang, F. Dong, M. Liu, H. Liu, Y. Zhang, C. Li, J. Gao, L. Bian, Nanocoral-like composite of nickel selenide nanoparticles anchored on two-dimensional multi-layered graphitic carbon nitride: a highly efficient electrocatalyst for oxygen evolution reaction, Appl. Catal. B 243 (2019) 463–469.

[39] Z. Fang, L. Peng, H. Lv, Y. Zhu, C. Yan, S. Wang, P. Kalyani, X. Wu, G. Yu, Metallic transition metal selenide holey nanosheets for efficient oxygen evolution electrocatalysis, ACS Nano 11 (2017) 9550–9557.

[40] M. Chen, Y. Zhang, R. Wang, B. Zhang, B. Song, Y. Guan, S. Li, P. Xu, Surface reconstruction of Se-doped NiS$_2$ enables high-efficiency oxygen evolution reaction, J. Energy Chem. 84 (2023) 173–180.

[41] H. Singh, M. Marley-Hines, S. Chakravarty, M. Nath, Multi-walled carbon nanotube supported manganese selenide as a highly active bifunctional OER and ORR electrocatalyst, J. Mater. Chem. A 10 (2022) 6772–6784.

[42] Y. Chang, P. Zhai, J. Hou, J. Zhao, J. Gao, Excellent HER and OER catalyzing performance of Se-vacancies in defects-engineered PtSe$_2$: from simulation to experiment, Adv. Energy Mater. 12 (2022) 2102359.

[43] S. Niu, W.-J. Jiang, Z. Wei, T. Tang, J. Ma, J.-S. Hu, L.-J. Wan, Se-doping activates FeOOH for cost-effective and efficient electrochemical water oxidation, J. Am. Chem. Soc. 141 (2019) 7005–7013.

[44] Y. Zuo, D. Rao, S. Ma, T. Li, Y.H. Tsang, S. Kment, Y. Chai, Valence engineering via dual-cation and boron doping in pyrite selenide for highly efficient oxygen evolution, ACS Nano 13 (2019) 11469–11476.

[45] H. Singh, W.P.R. Liyanage, M. Nath, Carbon nanotube encapsulated metal selenide nanostructures for efficient electrocatalytic oxygen evolution reaction, ChemComm 58 (2022) 8360–8363.

[46] J. Yu, G. Cheng, W. Luo, 3D mesoporous rose-like nickel-iron selenide microspheres as advanced electrocatalysts for the oxygen evolution reaction, Nano Res 11 (2018) 2149–2158.

[47] K. Ao, J. Dong, C. Fan, D. Wang, Y. Cai, D. Li, F. Huang, Q. Wei, Formation of yolk–shelled nickel–cobalt selenide dodecahedral nanocages from metal–organic frameworks for efficient hydrogen and oxygen evolution, ACS Sustain. Chem. Eng. 6 (2018) 10952–10959.

[48] Z. Wang, J. Li, X. Tian, X. Wang, Y. Yu, K.A. Owusu, L. He, L. Mai, Porous nickel–iron selenide nanosheets as highly efficient electrocatalysts for oxygen evolution reaction, ACS Appl. l Mater. Interfaces 8 (2016) 19386–19392.

[49] C. Lu, A. Li, G. Li, Y. Yan, M. Zhang, Q. Yang, W. Zhou, L. Guo, S-decorated porous Ti$_3$C$_2$ MXene combined with in situ forming Cu$_2$Se as effective shuttling interrupter in Na–Se batteries, Adv. Mater. 33 (2021) 2008414.

[50] K. Fan, H. Zou, Y. Lu, H. Chen, F. Li, J. Liu, L. Sun, L. Tong, M.F. Toney, M. Sui, J. Yu, Direct observation of structural evolution of metal chalcogenide in electrocatalytic water oxidation, ACS Nano 12 (2018) 12369–12379.

[51] F. Wang, P. Zou, Y. Zhang, W. Pan, Y. Li, L. Liang, C. Chen, H. Liu, S. Zheng, Activating lattice oxygen in high-entropy LDH for robust and durable water oxidation, Nat. Commun. 14 (2023), 6019-6019.

[52] N. Zhang, X. Feng, D. Rao, X. Deng, L. Cai, B. Qiu, R. Long, Y. Xiong, Y. Lu, Y. Chai, Lattice oxygen activation enabled by high-valence metal sites for enhanced water oxidation, Nat. Commun. 11 (2020) 466.

[53] J. Huang, Y. Li, Y. Zhang, G. Rao, C. Wu, Y. Hu, X. Wang, R. Lu, Y. Li, J. Xiong, Identification of key reversible intermediates in self-reconstructed nickel-based hybrid electrocatalysts for oxygen evolution, Angew. Chem. Inter. Ed. 58 (2019) 17458–17464.

[54] P. Zhai, M. Xia, Y. Wu, G. Zhang, J. Gao, B. Zhang, S. Cao, Y. Zhang, Z. Li, Z. Fan, C. Wang, X. Zhang, J.T. Miller, L. Sun, J. Hou, Engineering single-atomic ruthenium catalytic sites on defective nickel-iron layered double hydroxide for overall water splitting, Nat. Commun. 12 (2021) 4587.

[55] Z.-P. Wu, H. Zhang, S. Zuo, Y. Wang, S.L. Zhang, J. Zhang, S.-Q. Zang, X.W. Lou, Manipulating the local coordination and electronic structures for efficient electrocatalytic oxygen evolution, Adv. Mater. 33 (2021) 2103004.

[56] P.V. Pham, S.C. Bodepudi, K. Shehzad, Y. Liu, Y. Xu, B. Yu, X. Duan, 2D Heterostructures for ubiquitous electronics and optoelectronics: principles, opportunities, and challenges, Chem. Rev. 122 (2022) 6514–6613.

[57] F. Wang, Y. Zhang, J. Zhang, W. Yuan, Y. Li, J. Mao, C. Liu, C. Chen, H. Liu, S. Zheng, In situ electrochemically formed Ag/NiOOH/Ni$_3$S$_2$ heterostructure electrocatalysts with exceptional performance toward oxygen evolution reaction, ACS Sustain. Chem. Eng. 10 (2022) 5976–5985.

[58] F. Wang, Y. Li, R. Zhang, H. Liu, Y. Zhang, X. Zheng, J. Zhang, C. Chen, S. Zheng, H. L. Xin, Activating single-atom Ni site via first-shell Si modulation boosts oxygen reduction reaction, Small 19 (2023) 2206071.

[59] X. Zheng, B. Zhang, P. De Luna, Y. Liang, R. Comin, O. Voznyy, L. Han, F.P.G. de Arquer, M. Liu, D. Cao Thang, T. Regier, J.J. Dynes, S. He, H.L. Xin, H. Peng, D. Prendergast, X. Du, E.H. Sargent, Theory-driven design of high-valence metal sites for water oxidation confirmed using in situ soft X-ray absorption, Nat. Chem. 10 (2018) 149–154.

[60] F. Wang, R. Zhang, Y. Zhang, Y. Li, J. Zhang, W. Yuan, H. Liu, F. Wang, H.L. Xin, Modulating electronic structure of atomically dispersed nickel sites through boron and nitrogen dual coordination boosts oxygen reduction, Adv. Funct. Mater. 33 (2023) 2213863.